PHYSICAL REVIEW B **94**, 115164 (2016)

High-order harmonic generation in solids: A unifying approach

Tran Trung Luu[*] and Hans Jakob Wörner
Laboratorium für Physikalische Chemie, ETH Zürich, 8093 Zürich, Switzerland

(Received 17 June 2016; published 29 September 2016)

There have been several experimental reports showing high-order harmonic generation from solids, but there has been no unifying theory presented as of yet for all these experiments. Here we report on the systematic investigation of high-order harmonic generation within the semiconductor Bloch equations, taking into account multiple bands and relaxation processes phenomenologically. In addition to reproducing key experiments, we show the following: (i) Electronic excitations, direct-indirect excitation pathways, and relaxation processes are responsible for high-order harmonic generation and control using midinfrared drivers in zinc oxide. We describe an intuitive picture explaining a two-color experiment involving noninversion symmetric crystals. (ii) High-order harmonic generation can be considered as a general feature of ultrafast strong-field-driven electronic dynamics in solids. We demonstrate this statement by predicting high-order harmonic spectra of solids that have not been studied yet.

DOI: 10.1103/PhysRevB.94.115164

I. INTRODUCTION

The discovery of high-order harmonic generation (HHG) from gases [1–3] has led to a completely new field of research, which involves the control, metrology, and spectroscopy of microcosms [4] in the gas phase on an unprecedentedly fast time scale. Over the years, together with the development of high-power lasers, strong field physics and more specifically HHG have contributed substantially to the study of the fundamental properties of matter [5–8] as well as real-time visualization of atomic-scale dynamics [9–12]. High-order harmonic generation in gases has therefore paved the way for attosecond science [13].

Solid-state photonics, however, is still on a much slower time scale. Due to the inability of solids to tolerate strong fields, the coherently radiated photon energy range is limited. As a result, there is a constraint on the associated electronic time scale that one can study. Recently, by exerting strong fields that are close to or higher than the Coulombic field in the potential of solids, radiation from coherent photons in the form of high-order harmonics was observed from the terahertz, midinfrared, and ultimately the extreme ultraviolet region of the electromagnetic spectrum [14–16]. All of these works with HHG reaching and extending above 20 orders have laid the foundation for solid-state HHG, and they make it possible to bring important ideas and techniques of attosecond physics to the condensed phase.

Field-driven electronic dynamics in solids is a well-established aspect [17–19], and HHG from solids has been investigated and predicted [20–26] up to the visible range of the spectrum. Several classes of techniques have been used to investigate this interesting topic. Insight into field-driven electron dynamics in solids can be obtained by solving one-electron problems in a semiclassical model [16,20,22,27], solving the time-dependent Schrödinger equation (TDSE) [25,28,29], or solving many-body problems in the Hartree-Fock approximation with the semiconductor Bloch equations (SBEs) [15,17–19,21,30].

Although semiclassical models are approximate, they reveal a great deal by explaining the physics well in some experiments [14,16,27,31]. However, treating only the field-driven electronic motion in a band is not adequate since in any field-driven process, interband excitations should be taken into account as well. This problem can be readily solved by invoking a TDSE or SBEs. Nevertheless, while a solution of the TDSE contains rich information [28], it is not straightforward to include in addition dephasing by multielectron effects in an easy way, as one can do with the SBEs. On the other hand, more elaborate treatments can be employed, such as the *ab initio* approach, namely the time-dependent density-functional theory [32], which solves the time-dependent Kohn-Sham equation [33] instead of TDSE. However, even with this costly approach, extracting intuitive physical insights is not a trivial task.

In perfect crystalline solids, the acceleration theorem derived by Bloch [34] shows that under the influence of a constant electric field F_0, the electron wave packet will perform translational motion in $\mathbf{k}$ space, which corresponds to an oscillatory motion in real space. The associated frequency is $\omega_B = eF_0a/\hbar$, where e is the elementary charge, a is the lattice constant, and $\hbar$ is the reduced Planck constant. Even though Bloch oscillations have been observed experimentally in superlattices [35,36], applying this concept to conventional lattices was hindered by the small size of the lattice constant, the low damage threshold, and the ultrafast scattering found in solids [37]. Thanks to the intense, ultrafast terahertz pulses, Schubert *et al.* [15] have unambiguously demonstrated the generation of broadband high-order harmonics from the bulk of gallium selenide (GaSe) as well as its time-domain measurements [30], and they showed that dynamical Bloch oscillations and quantum interference of crystal electrons underlie its physical nature.

In the midinfrared regime, it has been demonstrated that high-order harmonics with photon energies lying above the band gap, with orders reaching up to 25, can be generated [14,27,31] by exposing zinc-oxide (ZnO) crystalline samples

---

[*] trung.luu@phys.chem.ethz.ch

to midinfrared laser pulses. The non-perturbative high-order harmonic emission in this case was interpreted as intraband excitations and later associated with a generalized recollision model [38].

In this work, we utilize the well-established multiband SBEs, which consistently take into account both inter- and intraband excitations as well as electronic relaxation processes. This analysis uses a similar model to the sophisticated multiband model of [15,30] while it applies to a variety of cases. This analysis also extends the model [38,39] used in previous experiments on ZnO since only a simple two-band model was used and hence no quantum interference of multiple bands was taken into account. As a result, we can not only reproduce the results of important experiments on GaSe [15] and HHG in ZnO [14], but we can also rigorously explain the pump probe results [38] from a different perspective. Further details as well as implications of these results are discussed.

The article is organized as follows: In Sec. II, we review and discuss the main theoretical formalisms used in this work. The semiconductor Bloch equations are written in full form. In Sec. III, we show the results that are obtained for different cases: (i) semiconductor driven by terahertz fields, (ii) semiconductor driven by midinfrared fields, (iii) prediction of high-order harmonic spectra from solids that have not been investigated yet. In Sec. IV, we summarize the conclusions and outline future prospects.

II. THEORETICAL APPROACH

The SBEs have already been derived and discussed in detail [17–19]. However, for the sake of convenience, and to assist in the follow-up analysis, we include in this section the complete equations, including the relaxation (scattering) terms. In the independent-particle approximation, the multiband equations describing the dynamics of interband coherence $p_{\mathbf{k}}^{\lambda,\lambda'}$ and populations of electrons $f_{\mathbf{k}}^{e}$ and holes $f_{\mathbf{k}}^{h}$ can be written in full as [15,17,30]

$$\begin{aligned}
i\hbar\frac{\partial}{\partial t}p_{\mathbf{k}}^{h_ie_j} &= \left(\mathcal{E}_{\mathbf{k}}^{e_j}+\mathcal{E}_{\mathbf{k}}^{h_i}-i\frac{\hbar}{T_2}\right)p_{\mathbf{k}}^{h_ie_j}-\left(1-f_{\mathbf{k}}^{e_j}-f_{\mathbf{k}}^{h_i}\right)\mathbf{d}_{\mathbf{k}}^{e_jh_i}\mathbf{E}(t)+i|e|\mathbf{E}(t)\nabla_{\mathbf{k}}p_{\mathbf{k}}^{h_ie_j}\\
&\quad+\mathbf{E}(t)\sum_{e_\lambda\neq e_j}\left(\mathbf{d}_{\mathbf{k}}^{e_\lambda h_i}p_{\mathbf{k}}^{e_\lambda e_j}-\mathbf{d}_{\mathbf{k}}^{e_je_\lambda}p_{\mathbf{k}}^{h_ie_\lambda}\right)+\mathbf{E}(t)\sum_{h_\lambda\neq h_i}\left(\mathbf{d}_{\mathbf{k}}^{h_\lambda h_i}p_{\mathbf{k}}^{h_\lambda e_j}-\mathbf{d}_{\mathbf{k}}^{e_jh_\lambda}p_{\mathbf{k}}^{h_ih_\lambda}\right),\\
i\hbar\frac{\partial}{\partial t}p_{\mathbf{k}}^{e_ie_j} &= \left(\mathcal{E}_{\mathbf{k}}^{e_j}-\mathcal{E}_{\mathbf{k}}^{e_i}-i\frac{\hbar}{T_2}\right)p_{\mathbf{k}}^{e_ie_j}+\left(f_{\mathbf{k}}^{e_j}-f_{\mathbf{k}}^{e_i}\right)\mathbf{d}_{\mathbf{k}}^{e_je_i}\mathbf{E}(t)+i|e|\mathbf{E}(t)\nabla_{\mathbf{k}}p_{\mathbf{k}}^{e_ie_j}\\
&\quad+\mathbf{E}(t)\sum_{e_\lambda\neq e_j}\mathbf{d}_{\mathbf{k}}^{e_\lambda e_i}p_{\mathbf{k}}^{e_\lambda e_j}-\mathbf{E}(t)\sum_{e_\lambda\neq e_i}\mathbf{d}_{\mathbf{k}}^{e_je_\lambda}p_{\mathbf{k}}^{e_ie_\lambda}+\mathbf{E}(t)\sum_{h_\lambda}\left(\mathbf{d}_{\mathbf{k}}^{h_\lambda e_i}p_{\mathbf{k}}^{h_\lambda e_j}-\mathbf{d}_{\mathbf{k}}^{e_jh_\lambda}\left(p_{\mathbf{k}}^{h_\lambda e_i}\right)^*\right),\\
i\hbar\frac{\partial}{\partial t}p_{\mathbf{k}}^{h_ih_j} &= \left(\mathcal{E}_{\mathbf{k}}^{h_i}-\mathcal{E}_{\mathbf{k}}^{h_j}-i\frac{\hbar}{T_2}\right)p_{\mathbf{k}}^{h_ih_j}+\left(f_{\mathbf{k}}^{h_i}-f_{\mathbf{k}}^{h_j}\right)\mathbf{d}_{\mathbf{k}}^{h_jh_i}\mathbf{E}(t)+i|e|\mathbf{E}(t)\nabla_{\mathbf{k}}p_{\mathbf{k}}^{h_ih_j}\\
&\quad+\mathbf{E}(t)\sum_{h_\lambda\neq h_j}\mathbf{d}_{\mathbf{k}}^{h_\lambda h_i}p_{\mathbf{k}}^{h_\lambda h_j}-\mathbf{E}(t)\sum_{h_\lambda\neq h_i}\mathbf{d}_{\mathbf{k}}^{h_jh_\lambda}p_{\mathbf{k}}^{h_ih_\lambda}+\mathbf{E}(t)\sum_{e_\lambda}\left(\mathbf{d}_{\mathbf{k}}^{e_\lambda h_i}\left(p_{\mathbf{k}}^{h_jh_\lambda}\right)^*-\mathbf{d}_{\mathbf{k}}^{h_je_\lambda}p_{\mathbf{k}}^{h_ie_\lambda}\right),
\end{aligned}\tag{1}$$

$$\begin{aligned}
\hbar\frac{\partial}{\partial t}f_{\mathbf{k}}^{e_i} &= \hbar\frac{\partial}{\partial t}f_{\mathbf{k}}^{e_i}\bigg|_{\text{relax}}-2\,\text{Im}\left[\sum_{e_\lambda\neq e_i}\mathbf{d}_{\mathbf{k}}^{e_ie_\lambda}\mathbf{E}(t)\left(p_{\mathbf{k}}^{e_\lambda e_i}\right)^*+\sum_{h_\lambda}\mathbf{d}_{\mathbf{k}}^{e_ih_\lambda}\mathbf{E}(t)\left(p_{\mathbf{k}}^{h_\lambda e_i}\right)^*\right]+|e|\mathbf{E}(t)\nabla_{\mathbf{k}}f_{\mathbf{k}}^{e_i},\\
\hbar\frac{\partial}{\partial t}f_{\mathbf{k}}^{h_i} &= \hbar\frac{\partial}{\partial t}f_{\mathbf{k}}^{h_i}\bigg|_{\text{relax}}-2\,\text{Im}\left[\sum_{h_\lambda\neq h_i}\mathbf{d}_{\mathbf{k}}^{h_\lambda h_i}\mathbf{E}(t)\left(p_{\mathbf{k}}^{h_ih_\lambda}\right)^*+\sum_{e_\lambda}\mathbf{d}_{\mathbf{k}}^{e_\lambda h_i}\mathbf{E}(t)\left(p_{\mathbf{k}}^{h_ie_\lambda}\right)^*\right]+|e|\mathbf{E}(t)\nabla_{\mathbf{k}}f_{\mathbf{k}}^{h_i}.
\end{aligned}\tag{2}$$

Here, $\lambda = e,h$ is the index, which specifies either an electron or a hole, $\mathcal{E}_{\mathbf{k}}^{e} = \mathcal{E}_{\mathbf{k}}^{c}$ and $\mathcal{E}_{\mathbf{k}}^{h} = -\mathcal{E}_{\mathbf{k}}^{v}$ are energies of the corresponding carriers in conduction or valence bands, T_2 is the dephasing period, and $\mathbf{d}_{\mathbf{k}}^{\lambda,\lambda'}$ is the dipole matrix element characterizing the transitions between the two bands λ,λ'.

In this analysis, we use a spin-independent Hamiltonian such that spatial inversion symmetry ($\mathcal{E}_{\mathbf{k}}^{\lambda} = \mathcal{E}_{-\mathbf{k}}^{\lambda}$) is obtained and $\mathcal{E}_{\mathbf{k}}^{\lambda}$ have zero slope at the boundaries of the Brillouin zone [40].

Note that in these equations, all the interactions leading to scattering effects beyond the mean-field approximation are characterized by either the $-i\frac{\hbar}{T_2}$ terms in Eq. (1) or the $\hbar\frac{\partial}{\partial t}f_{\mathbf{k}}^{\lambda_i}|_{\text{relax}}$ terms in Eq. (2). Because thermal equilibrium is usually achieved much faster in the presence of electron-electron (or electron-phonon) interactions rather than the intrinsic radiative lifetime of the carriers, employing phenomenological dephasing at this stage is a convenient choice. Furthermore, the relaxation terms still within the Markovian approximation in Eq. (2) can also be approximated as [30]

$$\hbar\frac{\partial}{\partial t}f_{\mathbf{k}}^{\lambda}\bigg|_{\text{relax}} = -\frac{1}{T_1}f_{\mathbf{k},A}^{\lambda},\tag{3}$$

with

$$f_{\mathbf{k},A}^{\lambda} = \frac{1}{2}\left[f_{\mathbf{k}}^{\lambda}-f_{-\mathbf{k}}^{\lambda}\right],\tag{4}$$

where T_1 represents the phenomenological damping of the antisymmetric part of the carriers. By declaring these terms, we can take into account both dephasing of the interband polarizations as well as scattering of intraband currents.

Since analytical solutions cannot be found for the SBEs with realistic experimental parameters [41–43], we solve the above set of equations numerically for arbitrary input parameters and for initially unexcited systems. For simplicity, we consider only one-dimensional band structure (justification is provided in Appendix A 2). Only the electric field, band-structure properties, and dephasing times T_2,T_1 are changed to represent several cases of recent key experiments. For SBEs with multiple bands the most time-consuming task is numerical integration of Eq. (1), thus the calculation time scales with the factor of $n(n-1)/2$. However, it scales nonlinearly with the electric field strength due to the required time step needed to converge the integration.

The total time-dependent interband polarization $\mathbf{P}(t)$ and intraband current density $\mathbf{J}(t)$ are given by

$$\mathbf{P}(t) = \sum_{\lambda,\lambda',\mathbf{k}} \big[\mathbf{d}_{\mathbf{k}}^{\lambda\lambda'} p_{\mathbf{k}}^{\lambda\lambda'}(t) + \text{c.c.}\big], \tag{5}$$

$$\mathbf{J}(t) = \sum_{\lambda,\mathbf{k}} -2|e| v_{\mathbf{k}}^{\lambda} f_{\mathbf{k}}^{\lambda}(t), \tag{6}$$

where $v_{\mathbf{k}}^{\lambda}$ is the group velocity of the λth band defined by $v_{\mathbf{k}}^{\lambda} = \nabla_{\mathbf{k}}\mathcal{E}^{\lambda}(\mathbf{k})/\hbar$. The total emitted spectral intensity can be calculated as

$$S(\omega) \propto |\omega\mathbf{P}(\omega) + i\mathbf{J}(\omega)|^2. \tag{7}$$

Furthermore, for the sake of simplicity, we consider only integration in one dimension, which corresponds to the most effective direction in the crystals. The direction consideration presented in the Appendix will show that this approximation is valid to a great extent. In addition, simplifying the wave equation to first order while neglecting the diffraction term results in the fact that the propagation can be approximated by simple multiplication of $S(\omega)$ with ω.

III. RESULTS

A. Semiconductors driven by terahertz pulses

As discussed before, the measurement of HHG from GaSe was interpreted as dynamical Bloch oscillations and quantum interferences of crystal electrons in multiple bands [15,30]. In this work, we show that their theoretical results can be reproduced by our analysis when we use the same GaSe band structure: three valence and two conduction bands in the Γ-K direction with which the laser polarization is aligned.

In our simulations, the input electric field was modeled as a Gaussian with a carrier frequency of 30.1 THz and a duration of 102.2 fs, as in [15]. Figure 1 shows clearly the generation of odd and even harmonics from GaSe extending beyond the 22nd order. Remarkably, the generation of even harmonics is maintained until the cutoff of the radiated spectrum. In addition, the relative intensities between the harmonics also are reproduced reasonably well. Here it is helpful to note that the quantum interference of crystal electrons is presented beautifully in the work of Hohenleutner *et al.* [30], including the supplementary information cited therein, and it was emphasized as a key role in breaking the inversion symmetry of GaSe, permitting the generation of the observed strong even harmonics. The strong couplings between the valence bands in GaSe [44] explain the importance of indirect excitation pathways in generating even harmonics in this particular material.

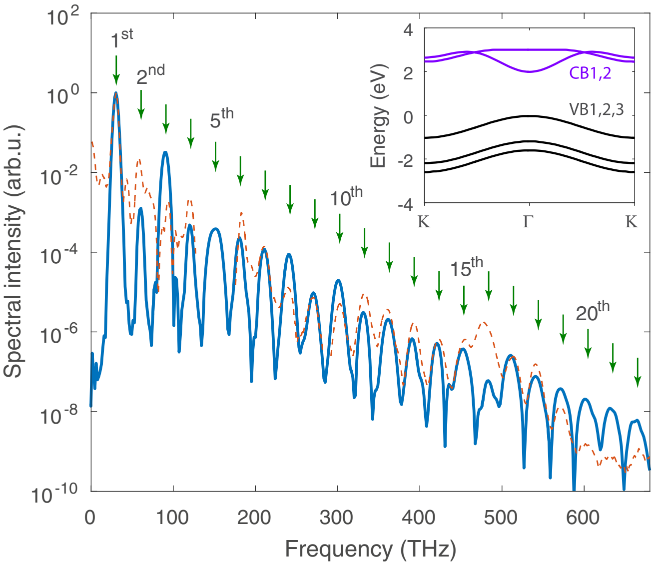

FIG. 1. High-order harmonic generation from a semiconductor driven by terahertz fields. Simulated spectral response of field-driven electron dynamics in GaSe (solid dark blue). Clear, strong even harmonics can be readily seen. The experimentally measured spectrum is shown by a dashed orange line [15]. The inset shows the model band structure, taken from [15], used in our simulation.

When we vary the input parameters and observe the change of the emitted HHG, a few conclusions can be drawn. First, changing the conduction-band structure results in only a minimal change in the emitted spectrum, but changing the valence-band structure results in a significant change. Second, changing the relaxation time of the antisymmetric part of the carriers has negligible consequences on the final observables. Third, the dephasing time of the interband polarization plays a crucial role, which is also discussed [39,45]. Not only can it smear out the high-order harmonic features in the total emitted spectrum, but it also correspondingly changes its intensity profile. The first two conclusions can be derived from the fact that the quantum interference between the valence bands is so strong that interband and intraband excitations in the conduction bands do not contribute high weight, but those from the valence bands do. The last conclusion is due to the dephasing-dependent nature of the total polarization that initiates all other types of excitation.

In addition to explaining the physics associated with the HHG from GaSe, the SBEs provide a strong foundation for several predictions: since the dephasing time has a substantial effect on the emitted spectra, by probing the intensity-dependent spectra carefully one would be able to extract collectively the phenomenological dephasing time associated with different excitation strengths. The dependence of the dephasing time with respect to the field strength results from the fact that the total electron-phonon scattering rate (acoustic phonons and longitudinal-optical phonons) increases as the electron energy increases [46]. Moreover, because the intensity envelope depends strongly on the structure of the valence bands and on their coupling, probing the emitted intensity profile as a function of the incident field strength might give rise to an all-optical characterization of the valence bands and their coupling in solids.

B. Semiconductors driven by midinfrared pulses

In this section, we present a different perspective to the existing discussions on the nature of HHG from ZnO [14,27,38]. Instead of emphasizing only interband polarization or generalized electron-hole recollision as the underlying physical process, our analysis shows that inter- and intraband excitations together with quantum interferences of crystal electrons in multiple bands are collectively responsible for the whole emission process.

In detail, it is important to note that ZnO is a noncentrosymmetric hexagonal wide-band-gap material that crystallizes preferentially in the wurtzite-type structure [47]. Therefore, second-order optical susceptibility exists and second-harmonic radiation can be generated from ZnO [48–51], as was indeed reported in the first work of Ghimire *et al.* [14]. However, as presented in the previous section and [15,30], it is not possible to account for even harmonics generated directly from crystalline ZnO only with a two-band model [38,39,45] and without a two-color-like electric field input. In detail, since there is only direct transition, quantum interference of direct and indirect transitions would not happen. The interband polarizations are inherently dominant over the total radiation because amplitude-wise, the intraband currents are very weak compared to the interband polarizations.

In an inversion-symmetric system, such as inert gas, even harmonics can still be generated by applying a second-harmonic electric field that breaks the symmetry of the incident field [52–55]. Nevertheless, the crystalline ZnO itself lacks inversion symmetry. Therefore, in the experiment [38] there are two competing processes: broken symmetry of the crystal itself and of the incident electric field. Our analysis can account for both of these processes, while the previous model [38,39,45] could not account for the first one, thus their interference was not included.

In our simulations, we use a band structure (shown in the Appendix) retrieved through conventional electronic structure software packages [56–58] with three conduction bands and five valence bands. The electric field polarization is chosen such that it is perpendicular to the polar hexagonal axis and parallel to the k_x axis (Γ-M direction in reciprocal space) [59]. The incident fundamental electric field is modeled as a Gaussian temporal profile with a width of 95 fs and a carrier wavelength of 3.76 μm [38]. The second-harmonic field is modeled with the same intensity envelope except that the carrier wavelength is doubled. The dephasing times are set at $T_1 = 100$ fs and $T_2 = 1$ fs. T_1 was found to be less influential than T_2. Now, we will show how quantum interference of the crystal electrons in the valence bands affects the traditional two-color control experiments and how the oscillation of even and odd harmonics would be changed with respect to that.

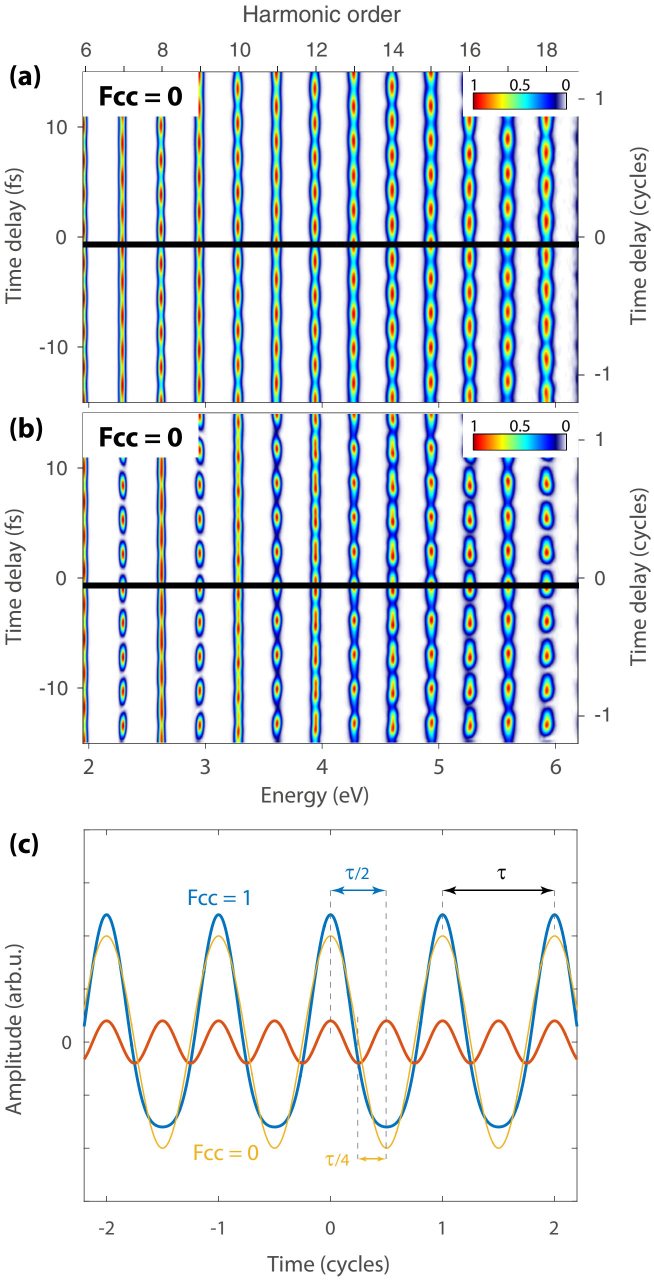

FIG. 2. Noninversion symmetric crystals break conventional two-color control of HHG. (a) Simulated spectral response of ZnO as a function of the delay between the fundamental and second-harmonic pulses. The intensity of the second-harmonic pulse is set to 5×10^{-3} times that of the fundamental pulse. All valence-band couplings are switched off, $F_{\mathrm{cc}} = 0$. Each harmonic is normalized independently. (b) The same delay-dependent spectral response calculated when the electric field of the second harmonic is increased three times. (c) Illustration of an intuitive explanation for HHG in inversion symmetric crystals (or inert gases) and noninversion symmetric crystals. The fundamental (second-harmonic) field is shown as the orange (red) solid line. The blue solid line is the resultant electric field ($F_{\mathrm{cc}} = 1$) due to interaction between the fundamental field and the noninversion-symmetric crystal.

Figure 2(a) shows a simulated two-color experiment in which quantum interference between the crystal electrons in the valence bands is switched off ($F_{\mathbf{cc}} = 0$). To facilitate a comparison with experimental results, all the energy ranges are selected to match reported data [38]. In this figure, several distinctive features can be seen: (i) these is a generation of both even and odd harmonics, (ii) the odd and even harmonics are out of phase for this particular second-harmonic intensity, and most importantly (iii) they oscillate four times per fundamental laser period. By increasing the second-harmonic intensity, one can demonstrate control of both odd and even harmonics such that they modulate in phase, as calculated in Fig. 2(b). All of these features are well known in gases [53,55]. However, in the experiment in solids [38], only the first two features are observed while the last feature is completely different: there are only two oscillations per fundamental laser period in the experiment.

Figure 2(c) provides an intuitive explanation for this experiment. In an inert gas (or solid material with inversion symmetry), the fundamental (solid orange line) and second-harmonic (solid red line) fields copropagate in the medium. When the delay between the two is varied, after a quarter of the fundamental period, i.e., after $\tau/4$, the coherently combined field will reach its maximum either upward or downward. As a result, four oscillations are expected per fundamental laser period τ for a delay map (generated spectrum as a function of the delay between the fundamental and second-harmonic electric field). In contrast, for a non-inversion-symmetric medium such as ZnO, the interaction of the fundamental laser pulse and the medium itself already generate a nonsymmetric electric field (solid blue line). Therefore, we can consider the competition between the two broken symmetries (of the medium and of the electric field) as the coherent effect generated due to a nonsymmetric electric field (solid blue line) and an incident second-harmonic pulse (solid red pulse). Clearly, because now the electric field is stronger upward rather than downward, the maximum field strength can only be achieved by varying the second-harmonic field delay half a fundamental laser period, i.e., $\tau/2$. As a result, two oscillations are expected per fundamental laser period, and this is what was observed in the experiment [38].

We proceed with our analysis by switching on the coherent control factor, $F_{\mathbf{cc}} = 1$. The results of this simulation for two different second-harmonic intensities are shown in Fig. 3. Indeed, when quantum interference is present, we observe two oscillations per fundamental laser period [Figs. 3(a) and 3(b)], which is confirmed by experiments. In addition, at low second-harmonic intensity [Fig. 3(a)], the harmonics shifts gradually from narrow to broad linewidths, which is also observed in the experiments (see Figs. 1 and 3 of Ref. [38]). Lastly, and most importantly, at higher second-harmonic intensity, almost all of the odd and even harmonics are in phase again [Fig. 3(b)], consolidating the control of HHG from semiconductors by a two-color field.

Simulations performed with identical parameters except for the different amplitude of the coherent control factor ($0 < F_{\mathbf{cc}} < 1$ and $F_{\mathbf{cc}} > 1$) exhibit similar results to those shown in Fig. 3. This suggests that while interference of interband excitations in the valence bands is very important, as shown above, the coherent control factor $F_{\mathbf{cc}}$ amplitude or the valence-band coupling strength is not very sensitive to a two-color experiment, therefore it would not be reconstructed by a two-color experiment. Further simulations are carried out in which we tune the band structure by adding a second spatial harmonics to the bands, $\mathcal{E}_{\mathbf{k}}^{\lambda} = \mathcal{E}_{\mathbf{k}}^{\lambda} + \sum_{n=0}^{2} \epsilon_{\lambda,n} \cos(nka)$, instead of using only $\mathcal{E}_{\mathbf{k}}^{\lambda}$ (here n is the order of spatial harmonic involved and a is the lattice constant). Strong control of the phase between odd and even harmonics is observed. In an analogous manner, we verified that a substantial change of the phase can also be obtained when we modify the dipole matrix elements from first-order $\mathbf{k} \cdot \mathbf{p}$ theory [17]. In conclusion, these observations point out that a two-color experiment might be able to shed light on the detailed structure of the bands as well as the dipole matrix elements. Reconstruction of these parameters could eventually be carried out with an appropriate model that rigorously and uniquely links the measurement results with the reconstructed parameters, which is different from [60].

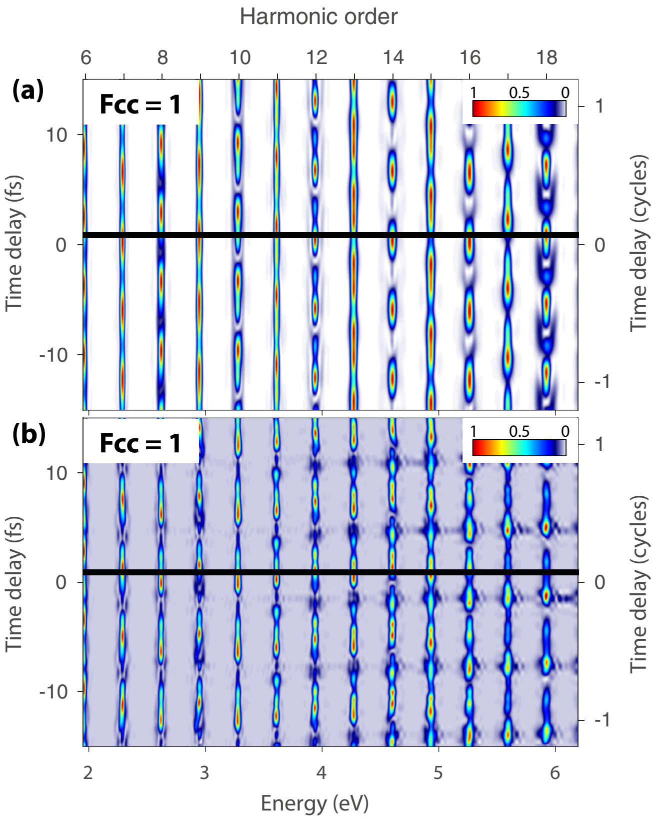

FIG. 3. Control of odd and even high-order harmonics by a two-color field. (a) Simulated spectral response of ZnO as a function of the delay between the fundamental and second-harmonic pulses. The intensity of the second-harmonic pulse is set at 2.5×10^{-3} times that of the fundamental pulse. Each harmonic is normalized independently. (b) Similar calculation performed for the same input parameters except that the second-harmonic field strength is increased five times. Gray solid lines show the same time delay when all the harmonics are out of phase (a) or in phase (b).

Although from the above analysis it can be concluded that electronic excitations (interband and intraband) together with quantum interference of crystal electrons in the valence bands are the source of HHG from ZnO, it is beneficial to extend the analysis to temporal and spectral properties of the generated HHG not only to reproduce previous work [14] but

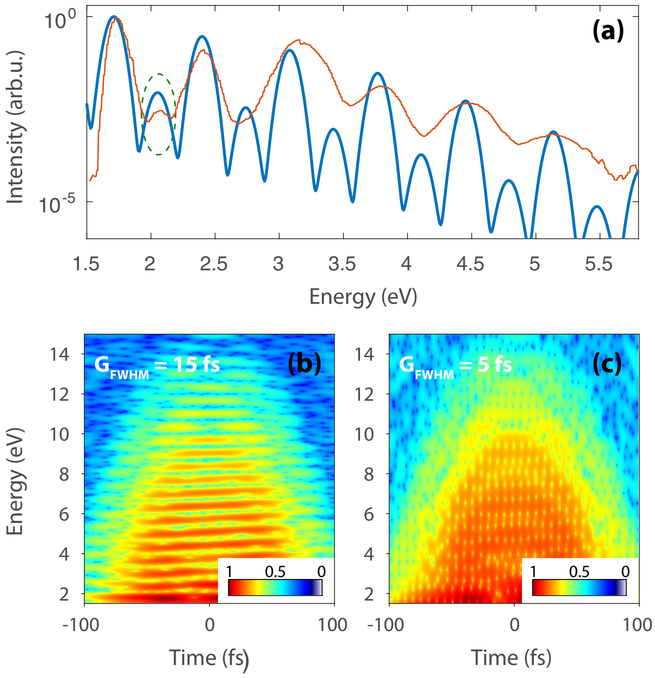

FIG. 4. Spectra and temporal characteristics of HHG from ZnO. (a) Simulated HHG spectrum of ZnO (solid dark blue line), plotted in the same spectral range as the experimental spectrum [14] (solid orange line). The oval dark green dashed line highlights the weak sixth-order harmonic that was also detected in experiment. (b) (Logarithmic scale) Time-frequency analysis of the generated temporal profile using a Gaussian with width $G_{\mathrm{FWHM}} = 15$ fs. (c) (Logarithmic scale) Same time-frequency analysis with a Gaussian width $G_{\mathrm{FWHM}} = 5$ fs.

also to support future work. Figure 4(a) shows the simulated spectrum emitted from field-driven ZnO, plotted in the range of the experiment (see Fig. 4 of Ref. [14]) using 3.62 μm as a carrier wavelength for the electric field. A high degree of agreement is obtained between the simulated result and the reported measurement. In particular, the existence of the even, weak sixth harmonic is well reproduced. To add clarity to the discussion involving interband or intraband as a dominant mechanism of HHG from solids [16,29,38], we performed a time-frequency analysis [29,61] on the temporal profile of the emitted radiation, and the results are shown in Figs. 4(b) and 4(c). To emphasize the importance of selecting the appropriate width of the temporal scanning window, two gate widths have been chosen: 15 and 5 fs. It can be seen that 5 fs is the proper selection since it does not create artificially high frequencies (compared to the case of 15 fs) and it can provide much higher temporal resolution than the other one. As a consequence, Fig. 4(c) corroborates the fact that the emitted radiation in ZnO can be attributed to both intra- and interband excitations. In contrast, Fig. 4(b) can be mistakenly considered as a step in favor of the intraband current as the dominating mechanism, which was proposed in the time-frequency analysis of [29].

C. High-order harmonic generation as a general feature of strong-field-driven solids

We found that the model band structures used in our analysis can be described also within the tight-binding approximation,

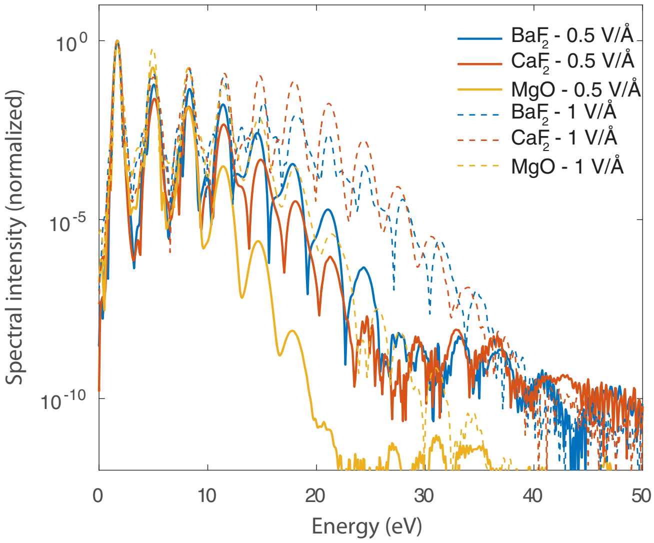

FIG. 5. HHG as a general feature of strong-field-driven solids. Simulated HHG spectra of different crystals being driven by different peak electric fields (shown in the legend). The crystal orientations are selected to have the maximum spectral response. In this case, they are all oriented such that the input laser polarization is parallel to Γ-L.

which still provided reasonable agreement with the experiments. Therefore, the treatment here can be generalized to many solids with similar properties. In other words, HHG could be a general feature that one could observe from ultrafast field-driven electronics in solids. Although there are a few experiments that reported HHG from solids, the materials are limited to GaSe, ZnO, and SiO_2. Here using the SBEs as a prediction tool, we perform a systematic comparison of HHG from high-band-gap materials that could possibly generate high-order harmonics similar to those in [16]. To extend the range of materials beyond semiconductors, we choose to investigate HHG from high-band-gap materials—barium fluoride (frankdicksonite, BaF_2), calcium fluoride (CaF_2), and magnesium oxide (MgO)—such that they allow nonlinear interactions with electric fields ranging from the near-infrared to the visible where there are abundant high-power laser sources.

The procedure of our analysis is described as follows: First, the electronic properties of the crystals are obtained (see the Appendix). Secondly, the SBEs are applied for different orientations at the same incident electric field for each individual crystal. Lastly, the combinations of crystal and orientation that have maximum spectral response are compared and plotted in Fig. 5.

The electric field is modeled as a Gaussian pulse with duration 5 fs, a carrier wavelength of 750 nm, and at two different peaks an electric field strength of 0.5 and 1 V/Å. In our analysis, for simplicity we chose to evaluate HHG only from crystal directions with a connection to the Γ valley: Γ-L, Γ-K, and Γ-X. The Γ-L direction dominates the spectral response in BaF_2 and CaF_2, while in MgO the dominance of Γ-L is not strong. From Fig. 5, several conclusions can be drawn: (i) all crystals exhibit a well-structured high-order harmonic signal extending beyond 20 eV. (ii) Although the crystals share the same symmetry (space group), HHG from the fluoride family is stronger than that from MgO at high energies. (iii) Extension of the HHG up to 40 eV is possible by increasing the electric field to 1 V/Å, which is well below the damage threshold of high-band-gap material exposed to ultrashort strong fields [16,62]. At high field strength, the HHG spectra develop a plateau that covers 30 eV bandwidth within four orders of magnitude in intensity, which should be accessible by a single experimental setup.

IV. CONCLUSIONS

In this detailed analysis, in addition to reproducing key experiments of HHG on solids [14,15,38], we have emphasized indirect excitation pathways as a key process in generating even harmonics from GaSe. Since the electronic dephasing and the band-structure affect the HHG spectra and its temporal profile, extraction of these parameters might be possible through detailed measurement of the characteristics of HHG from GaSe.

Furthermore, we proved unambiguously that there are two competing broken symmetries in the two-color experiments on ZnO, and a proper theoretical consideration must take both of them into account. We described a simple intuitive picture that explains their competition and the resultant change in oscillation period of the harmonics with respect to the two-color time delay. In addition, we verified that control of both even and odd harmonics in a two-color experiment can be elucidated through a combination of electronic excitations and interference of interband excitations. This collective behavior is corroborated by the time-frequency analysis of the temporal profile of the HHG from ZnO.

In all of our analyses here, an ultrafast dephasing time T_2 on the order of 1 fs was needed to obtain reasonable spectral and temporal characteristics of HHG as measured in the experiments. This suggests that dephasing and multielectron effects can be extremely fast even in semiconductors, indicating the need for their direct measurements in semiconductors. Since the SBEs utilized in this analysis provide a good quantitative description of HHG from solids, they can be further employed for reconstruction of electronic dephasing and other scattering effects.

HHG from solids is considered as a general feature of strong-field-driven solids. It is predicted that under exposure to few-cycle strong electric fields, BaF_2, CaF_2, and MgO will exhibit HHG, and the HHG spectra can be extended up to 40 eV by increasing the field strength to 1 V/Å. The HHG spectra should be scalable even to higher photon energy, under the maximum field strength defined by the damage threshold of the medium.

Although Coulomb interactions are not included in our treatment yet, it was shown in [41] that excitonic effects and Coulomb scattering play only one role in the weak-field regime. In the strong-field regime where the electric field inside the crystal reaches or exceeds the Coulomb potential (electric-field strength at the order of 1 V/Å), light-matter interaction has a dominant effect in the total optical response of the system, thus justifying our approach.

Our work shows that SBEs are a versatile tool in investigating electronic dynamics in solids. We demonstrate the unifying nature of this description, which covers well the whole spectral range from terahertz to vacuum ultraviolet radiation. The SBEs might also be a great tool to complement recent discovery of HHG from solid argon and krypton [63]. We anticipate that our work and the SBEs will help bridge the gap between solid-state photonics [19] with strong field laser physics [64] and attosecond science [13] through studies of HHG from solids with a broad spectrum of applications. Further studies of HHG from solids might benefit substantially from extending our current model beyond the Markovian approximation [17,19] by taking into account non-Markovian scattering processes. Experimentally, time-domain characterization of the HHG from solids [65] could help to verify theoretical studies. In addition, high-order harmonic spectroscopy in solids could serve as an important tool in determining the phase relaxation times that were measured previously via conventional techniques such as four-wave mixing experiments, Rayleigh scattering and speckle analysis, THz spectroscopy, etc. [19].

ACKNOWLEDGMENTS

We would like to thank Till Klostermann for his support. We gratefully acknowledge funding from an ERC Starting Grant (307270-ATTOSCOPE), the ETH Postdoctoral Fellowship Program (FEL-31 15-2), and the NCCR-MUST, a funding instrument of the Swiss National Science Foundation.

APPENDIX A: TECHNICAL DETAILS

1. Electronic properties of solids obtained from first-principles electronic structure calculation software

To supplement our proof-of-principle analysis, we extract electronic properties of GaSe and ZnO from first-principles electronic structure calculation software [56–58]. GaSe has a hexagonal structure, with the space group 194 and Hermann-Mauguin notation $P6_3/mmc$. Its lattice constants are $a = 3.742$ Å and $c = 15.919$ Å. The bulk configuration was calculated using a variety of exchange-correlation functionals within three approximations [66] [the local density approximation (LDA), the generalized gradient approximation (GGA), and the metageneralized gradient approximation (MGGA)]

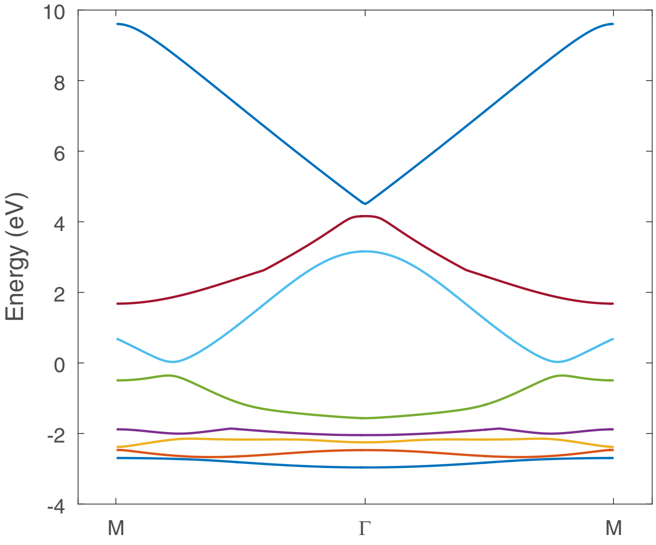

FIG. 6. ZnO band structure used in the simulations.

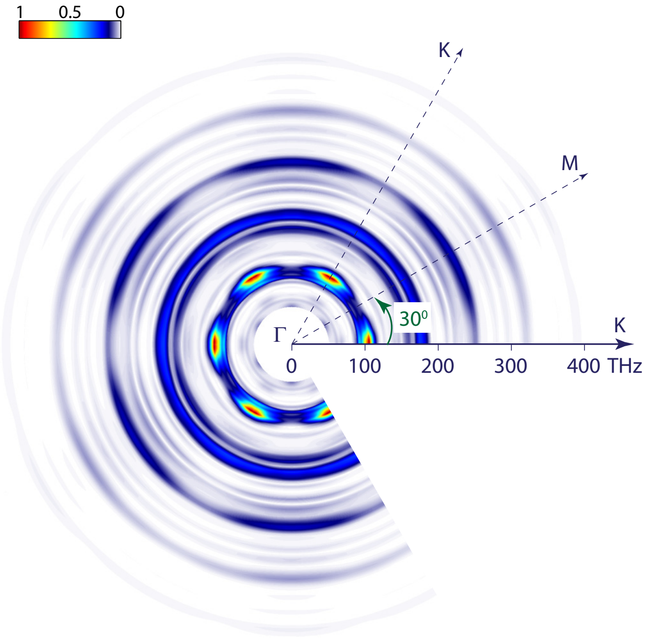

FIG. 7. Direction-dependent HHG from GaSe. Top: HHG spectra calculated for a different alignment angle of the input laser polarization with respect to the crystal orientation. The input laser polarization is initially oriented to the Γ-K direction, then it turns toward Γ-M and back to Γ-K. The sixfold symmetry of the crystal is clearly demonstrated.

and different parametrizations. A similar procedure is carried out for ZnO (wurtzites, hexagonal) with space group 186 and Hermann-Mauguin notation $P6_3mc$. Its lattice constants are $a = 3.2495$ Å and $c = 5.2069$ Å. BaF_2, CaF_2, and MgO share the same space group 225 and Hermann-Mauguin notation $Fm3m$ with the face-centered-cubic lattice. Their lattice constants are $a = 6.2$ Å, 5.462 95 Å, and 4.2112 Å, respectively.

For our calculations, as is well known, the change in band structure and correspondingly the dipole matrix elements due to increasing the grid size or reducing the convergence tolerance is much smaller than the changes induced by the use of different exchange correlation functionals or approximations.

Figure 6 shows the actual band structure with five valence bands and three conduction bands used in our simulations. The selection of bands is such that (i) they cover all the emission energy range in the experiments, and (ii) there are significant gaps to the next lower (higher) valence (conduction) bands. Few overlapping bands are removed to reduce simulation times while not affecting the final results. The dipole matrix elements are calculated using first-order $\mathbf{k} \cdot \mathbf{p}$ theory.

2. Appropriateness of 1D simulation: Direction consideration

A precise calculation of the field-driven electronic dynamics in solids at different directions of input polarization requires precise electronic properties of solids along the corresponding directions. In this analysis, we calculate the direction-dependent band dispersions directly from bulk configuration instead of interpolating the known band dispersions between different directions.

Figure 7 shows a simulated rotation experiment of HHG from GaSe. Input pulse parameters are taken from [30]. The peak electric field is set at 0.4 V/Å. The electronic structure properties are extracted directly using the above procedure utilizing the LDA with Perdew-Zunger parametrization. It is clear that in a low-energy range, the emitted radiation in the Γ-K direction is significantly stronger (more than one order of magnitude) than the radiation in the Γ-M direction, which is similar to other directions. Therefore, one-dimensional treatment of the SBEs is justified.

---

[1] A. McPherson, G. Gibson, H. Jara, U. Johann, T. S. Luk, I. A. McIntyre, K. Boyer, and C. K. Rhodes, J. Opt. Soc. Am. B **4**, 595 (1987).

[2] M. Ferray, A. L'Huillier, X. F. Li, L. A. Lompre, G. Mainfray, and C. Manus, J. Phys. B **21**, L31 (1988).

[3] A. L'Huillier and P. Balcou, Phys. Rev. Lett. **70**, 774 (1993).

[4] F. Krausz and M. Ivanov, Rev. Mod. Phys. **81**, 163 (2009).

[5] J. Itatani, J. Levesque, D. Zeidler, H. Niikura, H. Pépin, J. C. Kieffer, P. B. Corkum, and D. M. Villeneuve, Nature (London) **432**, 867 (2004).

[6] T. Remetter, P. Johnsson, J. Mauritsson, K. Varjú, Y. Ni, F. Lépine, E. Gustafsson, M. Kling, J. Khan, R. López-Martens, K. J. Schafer, M. J. J. Vrakking, and A. L'Huillier, Nat. Phys. **2**, 323 (2006).

[7] S. Baker, J. S. Robinson, C. A. Haworth, H. Teng, R. A. Smith, C. C. Chirila, M. Lein, J. W. G. Tisch, and J. P. Marangos, Science **312**, 424 (2006).

[8] D. Baykusheva, M. S. Ahsan, N. Lin, and H. J. Wörner, Phys. Rev. Lett. **116**, 123001 (2016).

[9] O. Smirnova, Y. Mairesse, S. Patchkovskii, N. Dudovich, D. Villeneuve, P. Corkum, and M. Y. Ivanov, Nature (London) **460**, 972 (2009).

[10] H. J. Wörner, J. B. Bertrand, D. V. Kartashov, P. B. Corkum, and D. M. Villeneuve, Nature (London) **466**, 604 (2010).

[11] E. Goulielmakis, Z.-H. Loh, A. Wirth, R. Santra, N. Rohringer, V. S. Yakovlev, S. Zherebtsov, T. Pfeifer, A. M. Azzeer, M. F. Kling, S. R. Leone, and F. Krausz, Nature (London) **466**, 739 (2010).

[12] P. M. Kraus, B. Mignolet, D. Baykusheva, A. Rupenyan, L. Horný, E. F. Penka, G. Grassi, O. I. Tolstikhin, J. Schneider, F. Jensen, L. B. Madsen, A. D. Bandrauk, F. Remacle, and H. J. Wörner, Science **350**, 790 (2015).

[13] P. B. Corkum and F. Krausz, Nat. Phys. **3**, 381 (2007).

[14] S. Ghimire, A. D. DiChiara, E. Sistrunk, P. Agostini, L. F. DiMauro, and D. A. Reis, Nat. Phys. **7**, 138 (2011).

[15] O. Schubert, M. Hohenleutner, F. Langer, B. Urbanek, C. Lange, U. Huttner, D. Golde, T. Meier, M. Kira, S. W. Koch, and R. Huber, Nat. Photon. **8**, 119 (2014).

[16] T. T. Luu, M. Garg, S. Y. Kruchinin, A. Moulet, M. T. Hassan, and E. Goulielmakis, Nature (London) **521**, 498 (2015).

[17] H. Haug and S. W. Koch, *Quantum Theory of the Optical and Electronic Properties of Semiconductors* (World Scientific, Singapore, 2003), p. 465.

[18] T. Meier, P. Thomas, and S. W. Koch, *Coherent Semiconductor Optics* (Springer, Berlin, 2007).
[19] C. F. Klingshirn, *Semiconductor Optics*, Vol. 53 (Springer, Berlin, 2012), p. 867.
[20] M. W. Feise and D. S. Citrin, Appl. Phys. Lett. **75**, 3536 (1999).
[21] D. Golde, T. Meier, and S. W. Koch, Phys. Rev. B **77**, 075330 (2008).
[22] O. D. Mücke, Phys. Rev. B **84**, 081202 (2011).
[23] D. Golde, M. Kira, T. Meier, and S. W. Koch, Phys. Status Solidi B **248**, 863 (2011).
[24] A. F. Kemper, B. Moritz, J. K. Freericks, and T. P. Devereaux, New J. Phys. **15**, 023003 (2013).
[25] P. G. Hawkins, M. Y. Ivanov, and V. S. Yakovlev, Phys. Rev. A **91**, 013405 (2015).
[26] P. G. Hawkins and M. Y. Ivanov, Phys. Rev. A **87**, 063842 (2013).
[27] S. Ghimire, A. D. DiChiara, E. Sistrunk, G. Ndabashimiye, U. B. Szafruga, A. Mohammad, P. Agostini, L. F. DiMauro, and D. A. Reis, Phys. Rev. A **85**, 043836 (2012).
[28] T. Higuchi, M. I. Stockman, and P. Hommelhoff, Phys. Rev. Lett. **113**, 213901 (2014).
[29] M. Wu, S. Ghimire, D. A. Reis, K. J. Schafer, and M. B. Gaarde, Phys. Rev. A **91**, 043839 (2015).
[30] M. Hohenleutner, F. Langer, O. Schubert, M. Knorr, U. Huttner, S. W. Koch, M. Kira, and R. Huber, Nature (London) **523**, 572 (2015).
[31] S. Ghimire, G. Ndabashimiye, A. D. DiChiara, E. Sistrunk, M. I. Stockman, P. Agostini, L. F. DiMauro, and D. A. Reis, J. Phys. B **47**, 204030 (2014).
[32] K. Yabana, T. Sugiyama, Y. Shinohara, T. Otobe, and G. F. Bertsch, Phys. Rev. B **85**, 045134 (2012).
[33] M. A. L. Marques, C. A. Ullrich, F. Nogueira, A. Rubio, K. Burke, and E. K. U. Gross, in *Time-Dependent Density Functional Theory*, edited by M. A. Marques, C. A. Ullrich, F. Nogueira, A. Rubio, K. Burke, and E. K. U. Gross, Vol. 706 (Springer, Berlin, 2006).
[34] F. Bloch, Z. Phys. **52**, 555 (1929).
[35] J. Feldmann, K. Leo, J. Shah, D. A. B. Miller, J. E. Cunningham, T. Meier, G. von Plessen, A. Schulze, P. Thomas, and S. Schmitt-Rink, Phys. Rev. B **46**, 7252 (1992).
[36] C. Waschke, H. G. Roskos, R. Schwedler, K. Leo, H. Kurz, and K. Köhler, Phys. Rev. Lett. **70**, 3319 (1993).
[37] A. Leitenstorfer, S. Hunsche, J. Shah, M. C. Nuss, and W. H. Knox, Phys. Rev. Lett. **82**, 5140 (1999).
[38] G. Vampa, T. J. Hammond, N. Thiré, B. E. Schmidt, F. Légaré, C. R. McDonald, T. Brabec, and P. B. Corkum, Nature (London) **522**, 462 (2015).
[39] G. Vampa, C. R. McDonald, G. Orlando, D. D. Klug, P. B. Corkum, and T. Brabec, Phys. Rev. Lett. **113**, 073901 (2014).
[40] M. S. Dresselhaus, G. Dresselhaus, and A. Jorio, *Group Theory* (Springer, Berlin, 2008).
[41] D. Golde, T. Meier, and S. W. Koch, J. Opt. Soc. Am. B **23**, 2559 (2006).
[42] T. Tritschler, O. D. Mücke, M. Wegener, U. Morgner, and F. X. Kärtner, Phys. Rev. Lett. **90**, 217404 (2003).
[43] M. Wegener, *Extreme Nonlinear Optics*, Advanced Texts in Physics (Springer-Verlag, Berlin, 2005), pp. 93–186.
[44] A. Segura, J. Bouvier, M. V. Andrés, F. J. Manjón, and V. Muñoz, Phys. Rev. B **56**, 4075 (1997).
[45] G. Vampa, C. R. McDonald, G. Orlando, P. B. Corkum, and T. Brabec, Phys. Rev. B **91**, 064302 (2015).
[46] M. V. Fischetti, D. J. DiMaria, S. D. Brorson, T. N. Theis, and J. R. Kirtley, Phys. Rev. B **31**, 8124 (1985).
[47] U. Ozgur, Y. I. Alivov, C. Liu, A. Teke, M. A. Reshchikov, S. Dogan, V. Avrutin, S.-J. Cho, and H. Morkoc, J. Appl. Phys. **98**, 041301 (2005).
[48] R. C. Miller, Appl. Phys. Lett. **5**, 17 (1964).
[49] G. Wang, G. K. L. Wong, and J. B. Ketterson, Appl. Opt. **40**, 5436 (2001).
[50] H. Cao, J. Y. Wu, H. C. Ong, J. Y. Dai, and R. P. H. Chang, Appl. Phys. Lett. **73**, 572 (1998).
[51] M. Lafrentz, D. Brunne, A. V. Rodina, V. V. Pavlov, R. V. Pisarev, D. R. Yakovlev, A. Bakin, and M. Bayer, Phys. Rev. B **88**, 235207 (2013).
[52] N. Dudovich, O. Smirnova, J. Levesque, Y. Mairesse, M. Y. Ivanov, D. M. Villeneuve, and P. B. Corkum, Nat. Phys. **2**, 781 (2006).
[53] X. He, J. M. Dahlström, R. Rakowski, C. M. Heyl, A. Persson, J. Mauritsson, and A. L'Huillier, Phys. Rev. A **82**, 033410 (2010).
[54] H. Eichmann, A. Egbert, S. Nolte, C. Momma, B. Wellegehausen, W. Becker, S. Long, and J. K. McIver, Phys. Rev. A **51**, R3414 (1995).
[55] U. Andiel, G. D. Tsakiris, E. Cormier, and K. Witte, Europhys. Lett. **47**, 42 (1999).
[56] P. Blaha, K. Schwarz, G. Madsen, D. Kvasnicka, and J. Luitz, *Karlheinz Schwarz* (Techn. Universität Wien, Austria, 2001).
[57] J. M. Soler, E. Artacho, J. D. Gale, A. Garcìa, J. Junquera, P. Ordejòn, and D. Sànchez-Portal, J. Phys. Condens. Matter **14**, 2745 (2002).
[58] M. Brandbyge, J.-L. Mozos, P. Ordejón, J. Taylor, and K. Stokbro, Phys. Rev. B **65**, 165401 (2002).
[59] M. I. Aroyo, J. M. Perez-Mato, D. Orobengoa, E. Tasci, G. De La Flor, and A. Kirov, Bulg. Chem. Commun. **43**, 183 (2011).
[60] G. Vampa, T. J. Hammond, N. Thire, B. E. Schmidt, F. Legare, C. R. McDonald, T. Brabec, D. D. Klug, and P. B. Corkum, Phys. Rev. Lett. **115**, 193603 (2015).
[61] V. S. Yakovlev and A. Scrinzi, Phys. Rev. Lett. **91**, 153901 (2003).
[62] M. Schultze, E. M. Bothschafter, A. Sommer, S. Holzner, W. Schweinberger, M. Fiess, M. Hofstetter, R. Kienberger, V. Apalkov, V. S. Yakovlev, M. I. Stockman, and F. Krausz, Nature (London) **493**, 75 (2012).
[63] G. Ndabashimiye, S. Ghimire, M. Wu, D. A. Browne, K. J. Schafer, M. B. Gaarde, and D. A. Reis, Nature **534**, 520 (2016).
[64] T. Brabec, in *Strong Field Laser Physics*, edited by T. Brabec, Vol. 134 (Springer, New York, 2009).
[65] M. Garg, M. Zhan, T. T. Luu, H. Lakhotia, T. Klostermann, A. Guggenmos, and E. Goulielmakis, Nature (London), doi: 10.1038/nature19821.
[66] C. Fiolhais, F. Nogueira, and M. Marques, *A Primer in Density Functional Theory* (Springer, Berlin, 2003).